Enabling Superior Cycling Stability of $LiNi_{0.9}Co_{0.05}Mn_{0.05}O_2$ with Controllable Internal Strain

Zhouliang Tan, Xiaoxuan Chen, Yunjiao Li, Xiaoming Xi, Shuaipeng Hao, Xiaohui Li, Xingjie Shen, Zhenjiang He, Wengao Zhao,* and Yong Yang**

Intergranular cracking of Ni-rich layered $LiNi_{1-x-y}Co_xMn_yO_2$ (1-x-y ≥ 0.8) cathode particles deteriorate the chemo–electro–mechanical stability of high-energy lithium-ion batteries (LIBs), thus presenting a challenge to typical modification methods to establish robust structures with highly efficient lithium-ion storage. Herein, the $ZrTiO_4$ (ZTO) as an epitaxial layer to enhance mechanical stability of ultrahigh-Ni $LiNi_{0.9}Co_{0.05}Mn_{0.05}O_2$ (NCM90) is reported for the first time. Intensive exploration from structure characterizations (X-ray absorption spectroscopy and in situ X-ray diffraction techniques), multi-physics field analysis, and first-principles calculations disclose that the conformal ZTO layers and Zr doping effectively suppresses the internal strain and the release of lattice oxygen, which prodigiously restrains the local stress accumulation during whole (de)lithiation processes, thereby maintaining good mechanical stability of the materials. Meanwhile, the protective ZTO layer also prevents electrolyte erosion, thus keeping an intact surface structure of NCM90. Notably, ZTO-modified NCM90 achieves significantly improved cyclability under high-voltage (4.5 V) operation, expressing a 17% increase in capacity retention (71% vs 88%) after 100 cycles. Overall, this work reveals the role of internal strain in the original degradation behavior and effectiveness of surface engineering strategy to solve the challenge, emphasizing that the conformal surface protection mitigates the internal stress of Ni-rich NCM by anchoring the lattice oxygen.

1. Introduction

Ni-rich layered NCM has gained big success in electric vehicle (EV) applications owing to environmental friendliness, extended lifespan, and high energy/power density.[1] The limited driving range and the high cost of EVs push the continuous development of higher capacity (energy density) NCM (Ni ≥ 0.8).[1b] However, the ultrahigh-Ni $LiNi_xCo_yMn_zO_2$ (x > 0.9) cathode still suffers from chemo–mechanical degradation and thermal stability issues in the long-term cycling and high-voltage operation,[2] resulting in thermal runaway and poor cycling life.

It is well known that the abrupt contraction of unit cell volume at high SOC (state of charge) directly affects the stability of the intrinsic structure of Ni-rich NCM cathodes, which leads to inhomogeneous local stress development inside the particles due to different variation orientations of the unit cell and primary particles, followed by the intragranular/intergranular cracking formation.[3] In addition to negatively affecting the structural integrity of the cathode particles, the new surfaces along the microcracks also suffer from electrolyte erosion and lead to more side reactions species accumulation.[4] As the cycling proceeds, the escape of lattice oxygen results in the formation of oxygen vacancies on the surface of NCM and subsequently induces oxygen release from the bulk structure.[5] The aforementioned phenomenon further induces Li^+/Ni^{2+} cation mixing, transition metal dissolution, and even the formation of the rock-salt phase,[6] ultimately leading to surface structural degradation and even the thermal runaway.

Effective modification strategies, such as lattice doping,[7] surface modification,[8] and core-shell structure design,[9] have been proposed to decelerate the structural decay of Ni-rich NCM. For example, Jamil et al. found that Nb-gradient doping enhances

Z. Tan, Y. Li, S. Hao, X. Li, X. Shen, Z. He
School of Metallurgy and Environment
Central South University
Changsha 410083, P. R. China
E-mail: yunjiao_li@csu.edu.cn
Z. Tan, Y. Li, S. Hao, X. Li, X. Shen, Z. He
Engineering Research Center of the Ministry of Education for Advanced Battery Materials
Central South University
Changsha 410083, P. R. China
X. Chen, Y. Yang
State Key Lab for Phys Chemistry of Solid Surfaces & Department of Chemistry
Xiamen University
Xiamen 361005, P. R. China
E-mail: yyang@xmu.edu.cn
X. Xi
Changsha Research Institute of Mining and Metallurgy
Changsha 410083, P. R. China
W. Zhao
Institute of Nanotechnology
Karlsruhe Institute of Technology (KIT)
76344 Eggenstein-Leopoldshafen, Germany
E-mail: wengao.zhao@kit.edu

the Li^+ transfer kinetic of single-crystal $LiNi_{0.8}Co_{0.1}Mn_{0.1}O_2$ through building a strong N—O bond,[10] resulting in excellent rate performance. Using a novel $LiFePO_4$@C nanoplate coating, Hu's group could improve the structural stability of $LiNi_{0.6}Co_{0.2}Mn_{0.2}O_2$ when cycling up to 4.6 V.[11] The main reason was that the preferential adsorption of PO_4^{3-} on the surface of the transition metal site (Ni, Co, and Mn) prevents the electrolyte catalytic oxidation and stabilizes the local structure of the transition metal ions and oxygen ions. In addition, Liu et al. constructed a polymer coating (3,4-ethylenedioxythiophene, PEDOT) on the surface of a single-crystal $LiNi_{0.83}Mn_{0.1}Co_{0.07}O_2$ cathode to increase the surface integrity by inhibiting electrode attack. However, when encountering the destruction issues of the layered structure led by lattice stress accumulation, these modification strategies often neglect the escape of lattice oxygen. To offer a theoretical basis for the design of next-generation Ni-rich cathode materials that combine high structural stability and energy density, it is indispensable to deeply understand the correlation among the lattice oxygen, internal strain, and structural stability on a microscopic scale.

In this work, an active ceramic material of ZTO was constructed on ultrahigh-Ni NCM90 by an in situ modification strategy. An epitaxial ZTO coating relieves the internal strain originating from lattice distortion and inhibits the release of lattice oxygen at high cutoff voltages, ensuring the structural integrity of the NCM90 cathode upon cycling. This work proposes reliable surface modification engineering to simultaneously suppress the internal strain and lattice oxygen release of the NCM90 cathode, thereby achieving superior cycling stability under high-voltage operation.

2. Results and Discussion

2.1. Structural Characterization of NCM90@ZTO-x

To obtain crystallographic structure information of the NCM90@ZTO-x, XRD patterns were collected (**Figure 1**a). All characteristic peaks of the samples can be clearly assigned to the hexagonal layered α-$NaFeO_2$ structure, accompanied by R-3m space group (JCPDS No. 70–4314),[12] demonstrating that there is no visible effect of the ZTO coating toward the bulk crystal structure of NCM90@ZTO-x cathodes. Additionally, an orderly arranged layered structure of the NCM90@ZTO-x can also be confirmed by the clear splitting of the (006)/(102) and (018)/(110) doublets. However, the characteristic peak (003) shifts to lower angles (Figure 1b), thus indicating c-axis expansion caused by the intercalation of additional ions into the lattice. To understand the lattice-coherent interface formation between ZTO coating and the bulk NCM90@ZTO-x cathodes, the interfacial binding energy was determined by first-principles calculations in Figure 1c. The results for the adhesion (W_{ad}) of ZTO(111)/NCM(003) and ZTO(011)/NCM(104) are −1.42 and 1.49 J m^{-2}, respectively, indicating a strong binding affinity and chemical interaction between ZTO and $LiNi_{0.9}Co_{0.05}Mn_{0.05}O_2$. Subsequently, XPS was performed on the Zr 3d and Ti 2p to

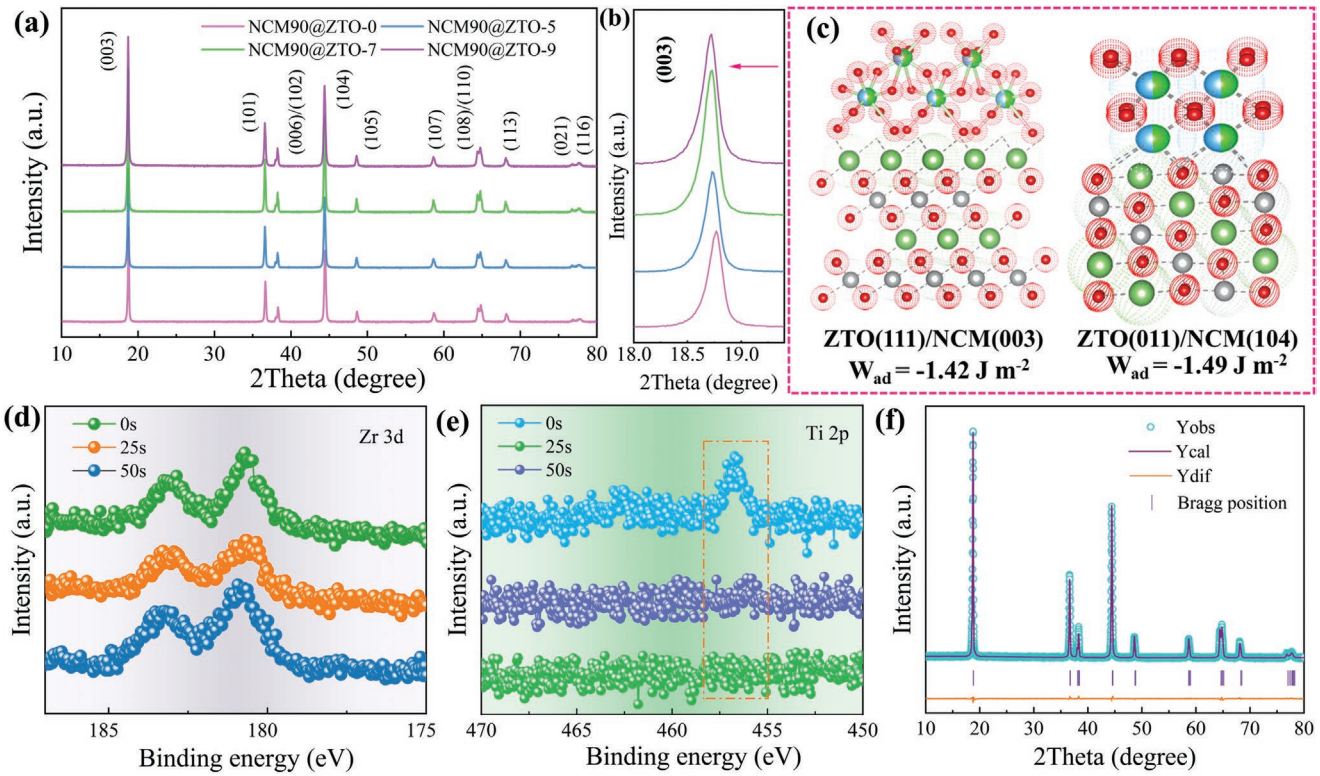

Figure 1. XRD patterns of a) NCM90@ZTO-x with enlarged views of b) (003) peaks. c) Simulation of the interfacial structure and the W_{ad} of ZTO (111)/NCM (003) and ZTO (011)/NCM (104). XPS pattern of d) Zr 3d and e) Ti 2p etched at different times. f) Rietveld refinements of XRD patterns for NCM90@ZTO-7.

detect the elemental composition of NCM90@ZTO-7. As shown in Figure 1d,e, the signals of the Zr and Ti elements appear on the surface of NCM90@ZTO-7 particles. In contrast, there is no visible Ti signal while the Zr maintains a strong peak in the etched sample. The result confirms that Ti element is more inclined to enrich on the particle surface because of the favorable interlayer affinity between ZTO and NCM.[13] Furthermore, first-principles calculations were carried out to unveil the localization of elements (Zr and Ti) in the lattice structure by tracking the elements replacement energy (Ere) in different layers. The calculation model and exact data are shown in Figures S1 and S2 (Supporting Information). It is clear that the Ti exhibits a lower Ere on the surface while the Zr displays a lower energy in the third layer, well consistent with the element locations of etched XPS results. Combining the first-principles calculations, the crystallographic model of the ZTO-NCM90 is exhibited in Figure S3 (Supporting Information), where the Ti element tends to aggregate on the surface to form a ZTO coating layer, while the Zr element replaces the transition metal sites in the lattice structure.

To verify the obtained crystallographic information, Rietveld refinements of XRD patterns for the NCM90@ZTO-x were performed in Figure 1f and Figure S4 (Supporting Information), where Zr ions in the TM (3b) site of the layered α-$NaFeO_2$ structure was constrained. All related parameters for the NCM90@ZTO-x samples are listed in Table S1 (Supporting Information), and the R_p and R_{wp} factors of all samples were below 4.5%, manifesting the reliability of the refinement results.[14] The Li^+/Ni^{2+} cation mixing of NCM90@ZTO-0, NCM90@ZTO-5, NCM90@ZTO-7, and NCM90@ZTO-9 was confirmed to be 4.90%, 3.89%, 3.22%, and 3.02% respectively, signifying the mitigation effect due to the ZTO modification, which is consistent with the trend of the $I_{(003)}/I_{(104)}$ intensity ratio of the NCM90@ZTO-x cathodes. Furthermore, as cation mixing occurs, the NCM90@ZTO-7 shows an ΔE(Li/Ni) of 1.12 eV, much higher than that of NCM90@ZTO-0 (0.86 eV), indicating that ZTO modification helps inhibit the nickel migration. The phenomenon can be attributed to the partial occupation of transition metal sites by zirconium. As opposed to nickel and cobalt, zirconium holds a more delocalized d orbit, which enhances the interaction between the transition metal layers and thereby effectively inhibits the migration of divalent nickel to the adjacent lithium layer.[15] In Figure S5 (Supporting Information), the signals of Ni 2p located at 854.8 eV and can be divided into Ni^{2+} and Ni^{3+} cations,[16] respectively. The Ni^{2+} concentration ratio of the NCM90@ZTO-7 is 0.58, much lower than that of the NCM90@ZTO-0 (0.78), which is mainly ascribed that more lattice O stabilizes the charge balance to prevent the reduction of trivalent nickel, thus anchoring more trivalent nickel on the surface of ZTO modified NCM90.[17] Apart from that, the oxygen vacancies generated during the calcination process lead to the TM ion migration.[18] Surprisingly, the O occupancy of ZTO-modified NCM90 significantly increased from 94.32% of the NCM90@ZTO-0 to 98.35% of the NCM90@ZTO-7, demonstrating an enhanced crystal structure. Moreover, the TM and Li slab thickness can be obtained from the refinement results (Table S2, Supporting Information).[19] The ZTO-modified NCM90 shows a significantly increased Li slab thickness compared to the unmodified one, attributed to the Coulomb repulsion reduction between the adjacent lithium layers originating from the larger attraction of Zr to the adjacent oxygen. Hence, the ZTO-modified NCM90 should show enhanced Li-ion migration kinetics, which positively affects the electrochemical performance. In summary, the ZTO-modification strategy can not only effectively suppress the cation mixing, but also regulate the oxygen vacancy formation in the Ni-rich NCM cathode.

It is typically crucial for Ni-rich layer oxides to have a spherical morphology to improve their energy and tap density. As represented in the SEM images of the NCM90@ZTO-x in Figure S6a–d (Supporting Information), all samples show similar spherical particles with a diameter of ≈9.5 µm, composed of compact primary particles. Furthermore, as indicated by EDS mapping of the NCM90@ZTO-7 in Figure S6e (Supporting Information), the elements of Ni, Co, Mn, O, Zr, and Ti show a uniform distribution, declaring a uniformly coated ZTO on the particle surface. Further, the focused ion beam (FIB) equipment was adopted to obtain a cross-sectional particle for detecting the distribution of the doping elements inside the particle in Figure S7 (Supporting Information). Compared with the NCM90@ZTO-0, the Zr element distributes inside the NCM90@ZTO-7 particle. **Figure 2**a–d illustrates the detailed crystal structure of the NCM90@ZTO-x as determined by HRTEM and Fourier transformation analysis. The HRTEM image (brown square, the selected region I) of the NCM@ZTO-0 sample (Figure 2a–b) displays a precise lattice fringe spacing of 4.73 Å, corresponding to the (003) plane of the layered structure.[20] It is worth noting that an epitaxial ZTO coating layer compactly anchors on the outer surface of the NCM@ZTO-7 particles, while the bulk region still presents an ordered layered structure (Figure 2c). Specifically, there are two types of lattice fringes of 2.93 and 4.76 Å observed in Figure 2d, which refers to the (111) plane of ZTO and the (003) plane of layered NCM cathode,[21] respectively. This observation confirms the ZTO coating has been successfully constructed on the free surface of the $LiNi_{0.9}Co_{0.05}Mn_{0.05}$ cathode.[22] It is noteworthy that there is a significant increase in the interlayer spacing thickness along the *c*-axis, originating from the larger ionic radius of Zr^{4+}, which further confirms its incorporation into the lattice structure of $LiNi_{0.9}Co_{0.05}Mn_{0.05}O_2$ (Table S2, Supporting Information), consistent with the theoretical calculation and the XRD refinement results.

To further assess the influence of the ZTO modification strategy toward the oxygen vacancies (VOs) in layered structures (**Figure 3**a,d), the etched-depth O 1s XPS of the different samples was explored, where there are three characteristic peaks at 533.5, 530.5, and 529.5 eV, assigned to chemical adsorption oxygen (O1), oxygen vacancies (O2), and lattice oxygen (O3),[23] respectively. Compared to the NCM90@ZTO-0, a higher intensity peak of O3 is clearly observed on the surface of NCM90@ZTO-7 (Figure 3b,c), which comes from the ZTO modification layer. With the increasing of etching depth from 0 to 10/50 nm (Figure 3e,f; Figure S8, Supporting Information), a higher integral area of O3 peaks for NCM90@ZTO-7 is still clearly remained in comparison to the NCM90@ZTO-0, indicating an active ZTO surface modification is beneficial to anchor the lattice O in the crystal structure of NCM90@ZTO-7. Less content of O3 in the subsurface of NCM90@ZTO-0 particle can be attributed to surface oxygen vacancy structure that triggers the

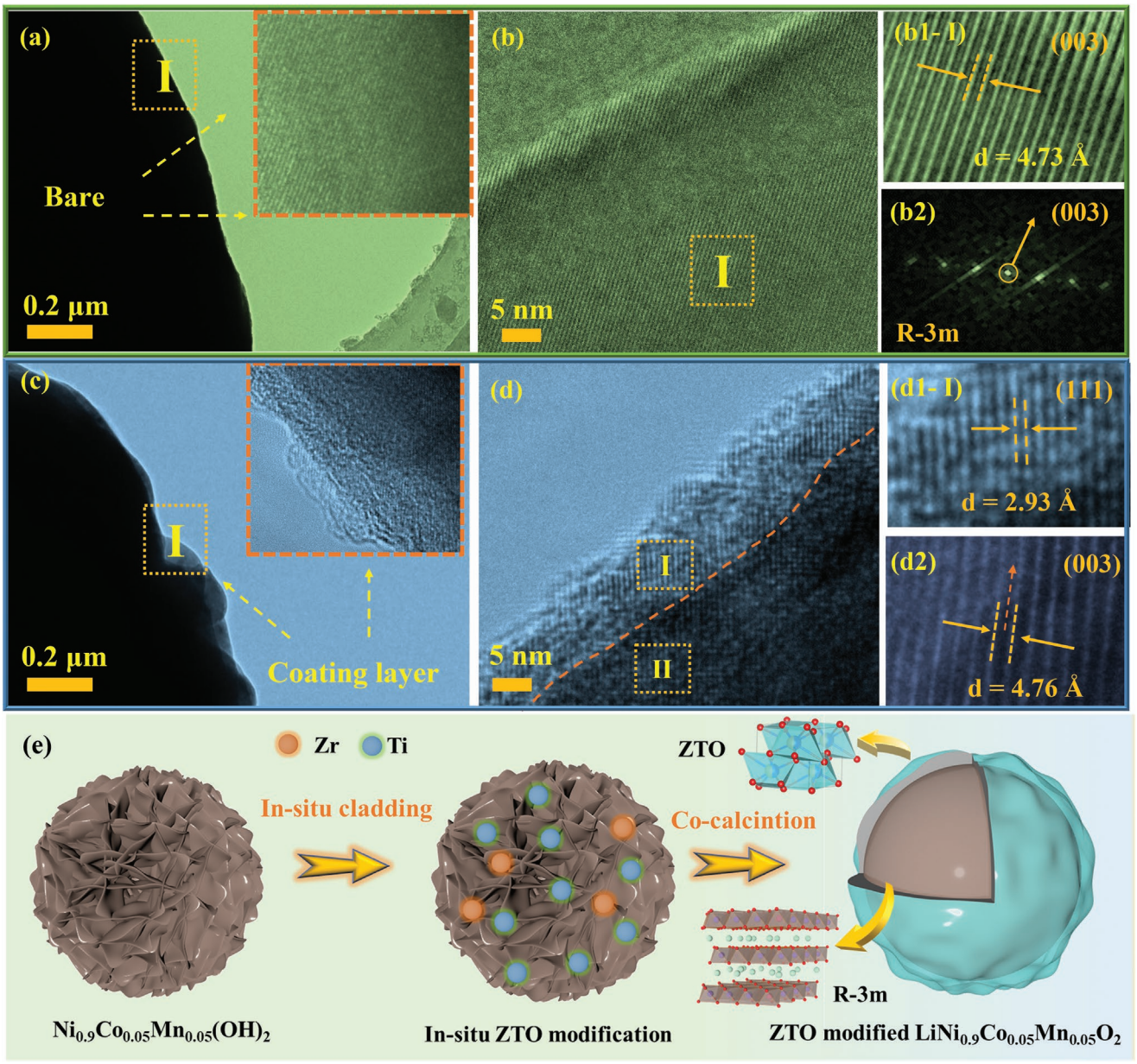

Figure 2. HRTEM images of a,b) NCM90@ZTO-0 and c,d) NCM90@ZTO-7. e) The synthesis diagram of ZTO-modified $LiNi_{0.9}Co_{0.05}Mn_{0.05}O_2$.

outward migration of oxygen in the bulk phase structure,[5a,24] ultimately resulting in the consecutive structure defect. Furthermore, electron paramagnetic resonance measurements of NCM90@ZTO-0 and NCM90@ZTO-7 were performed (Figure 3g). A sharper peak intensity appears in the NCM90@ZTO-0 sample compared to NCM90@ZTO-7, attributed to the generation of more VOs during heat treatment, in line with the results from Rietveld refinements and XPS.

To investigate the charge-compensation mechanism associated with oxygen vacancies, TM (Ni, Co, and Mn) L-edge and O K-edge soft XAS was carried out. The Ni, Co, and Mn d K-edge XAS spectra are presented in Figure 3h,i and Figure S9 (Supporting Information). It is noticeable that the difference in Ni L-edge between NCM90@ZTO-0 and NCM90@ZTO-7 is conspicuous, indicating the local structure variation after ZTO modification. The intensity of Ni L-edge spectra is significantly enhanced, and shifts to higher energy, suggesting the less antidivalent nickel and a lower cation mixing of the NCM90@ZTO-7.[25] The Co and Mn L-edge XAS spectra display a similar trend with Ni spectra, demonstrating a slight change in the local environment (Figure S9, Supporting Information). Moreover, the O K-edge shows several characteristic peaks in the green and purple regions, which originate from the horizontal transition of electrons from the O 1s core to the hybridization of the O 2p orbitals with the 3d and 4sp orbitals of TM,[26] respectively. A significantly decreased intensity is observed after ZTO modification in the green region because of fewer oxygen vacancies,[27] which is consistent with the XPS results. Overall,

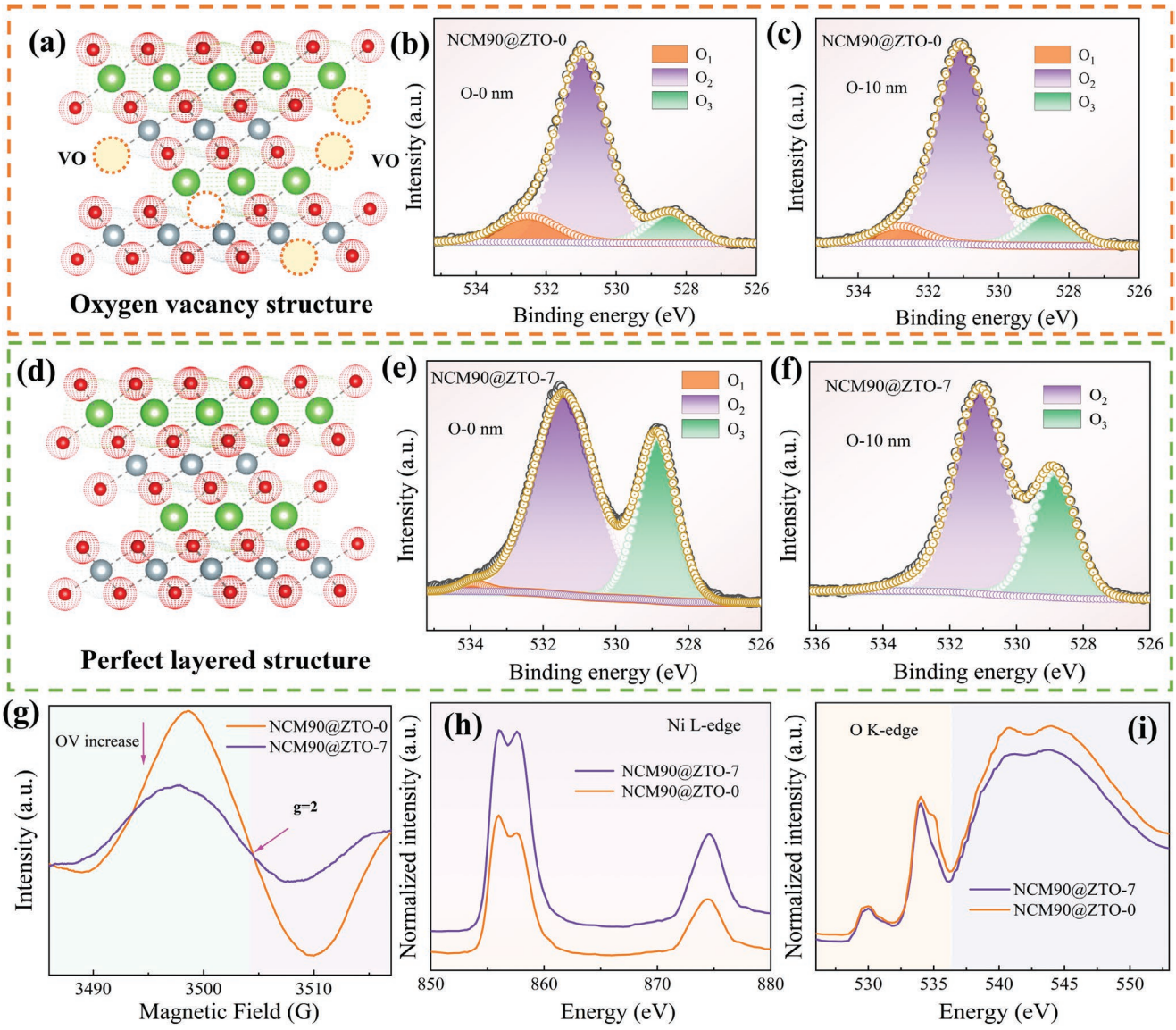

Figure 3. a,d) Schematic of oxygen-vacancy structure and perfectly layered structure. The etched-depth XPS of O 1s for(b,c) NCM90@ZTO-0 and e,f) NCM90@ZTO-7. g) EPR spectra of NCM90@ZTO-0 and NCM90@ZTO-7 and XAS spectra of the h) Ni-L edge and i) O-K edge.

an ultrahigh-Ni NCM with a stable lattice oxygen structure is achieved by building a robust ZTO modification layer, indicating a promising strategy to maintain the local structural integrity of the cathode.

2.2. Electrochemical Performance of NCM90@ZTO-X Cathodes

The electrochemical performances of the NCM90@ZTO-x cathodes were recorded to verify the effect of the ZTO modification strategy in **Figure 4**. All cells show similar charge/discharge curves and discharge capacities (Figure 4a; Figure S10, Supporting Information). The average specific discharge capacities of NCM90@ZTO-0, NCM90@ZTO-5, NCM90@ZTO-7, and NCM90@ZTO-9 are 215.4, 215.4, 216.1, and 215.0 mAh g^{-1} with the average Coulombic efficiency (η) of 81.33, 81.40, 84.09, and 82.54% (Figure S11, Supporting Information), respectively. The enhanced initial η of the ZTO-modified NCM90 benefits from the improved stability and reduced residual Li on the surface of NCM90 (Figure S12, Supporting Information).[5c,28] Figure 4b displays the rate capability of the NCM90@ZTO-x cathodes tested at different C-rates (1C = 200 mA g^{-1}) and then switched to 0.5 °C for 70 cycles. Note that the ZTO-modified NCM90 cathodes deliver higher specific capacity than the pristine NCM90 cathode. With increasing current density, such discrepancy becomes more apparent. Notably, the NCM90@ZTO-7 cathode maintains a specific capacity of 198.5 mAh g^{-1} at 5 °C and 173.9 mAh g^{-1} at 10 °C, superior to that of NCM90@ZTO-0 cathode (165.3 mAh g^{-1} at 5 °C and 157.2 mAh g^{-1} at 10 °C). Furthermore, the NCM90@ZTO-7 cathode keeps a specific capacity of 198.5 mAh g^{-1} after 100 cycles while the cycling rate switches to 0.5 °C, whereas the

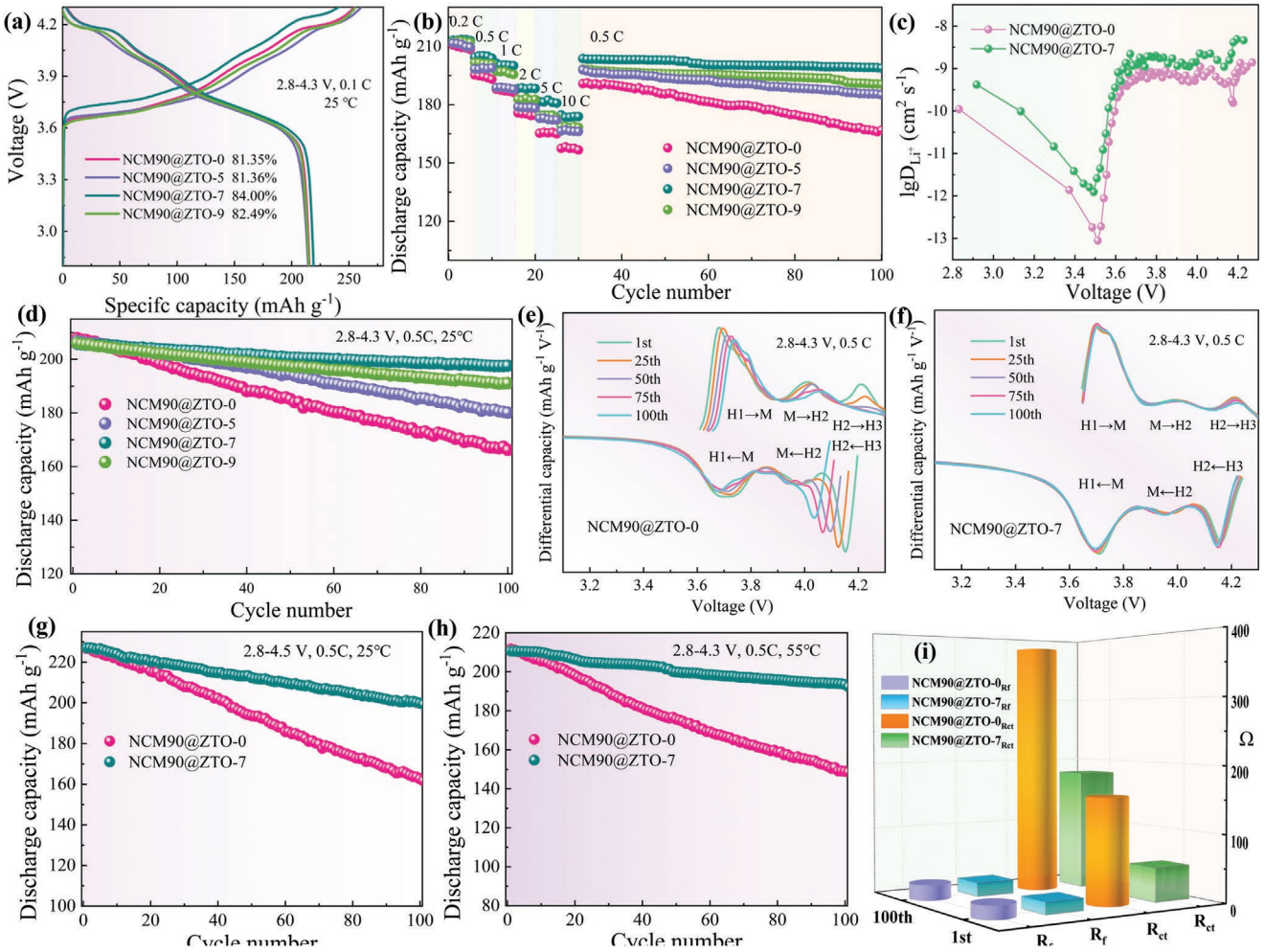

Figure 4. a) The charge/discharge curves of all cathodes for the first cycle. b) Rate capability, c) lithium-ion diffusion rate (D_{Li+}) and d) cycling performance of the NCM90@ZTO-x conducted at 25 °C in the range of 2.8–4.3 V. e,f) dQ dV^{-1} profiles, g) cycling performance conducted at 25 °C in the range of 2.8–4.5 V, h) cycling performance at 55 °C in the range of 2.8–4.3 V and i) fitting data of Nyquist plots for NCM90@ZTO-0 and NCM90@ZTO-7.

NCM90@ZTO-0 cathode fades to 166.3 mAh g^{-1} after 100 cycles. The enhanced rate capability of ZTO-modified sample is probably due to its increased Li slab thickness and stable lattice, thus guaranteeing smooth Li^+ transfer. Furthermore, the GITT and CV tests were conducted to deeply understand the influence of the ZTO surface modification toward the Li-ion diffusion kinetic (Figure S13a,b and Figure S14, Supporting Information). As shown in the comparison of the D_{Li^+} between NCM90@ZTO-0 and NCM90@ZTO-7 cathodes in Figure 4c, calculated from the GITT data,[29] the D_{Li^+} exhibits a dynamic change due to the variation of the Li-ion diffusion barrier and shows a sharp drop at 3.55 and 4.2 V in the delithiation process, corresponding to the internal strain generation during the phase transformation (H1-M, H2-H3). It is noteworthy that the NCM90@ZTO-7 consistently keeps a higher D_{Li^+} value than the pristine NCM90@ZTO-0, indicating enhanced lithium-ion diffusion kinetics consistent with the results from CV testing (1.4×10^{-11} cm^2 s^{-1} for NCM90@ZTO-7 vs 9.0×10^{-12} cm^2 s^{-1} for NCM90@ZTO-0). Obviously, the enhanced lithium-ion diffusion kinetics of ZTO-modified samples accounts for the outstanding rate capability even under the harsh current density of 10 °C.

Figure 4d displays a longer cycle performance of the NCM90@ZTO-x at 0.5 C in the voltage range of 2.8–4.3 V. It is found that all ZTO-modified NCM90 deliver higher capacities than the pristine NCM@ZTO-0. The discharge capacity of the NCM@ZTO-0 cathode suffers from rapid decay (Figure S15a, Supporting Information), decreasing from 207.9 mAh g^{-1} to 165.2 mAh g^{-1} with a capacity retention of only 79.4% after 100 cycles. In contrast, the NCM90@ZTO-7 cathode delivers the highest discharge capacity of 197.6 mAh g^{-1}, corresponding to a capacity retention of 96.0% (Figure S15b, Supporting Information). The enhanced cycling performance of ZTO-modified NCM90 stems from the improved (surface) lattice structural integrity, thereby suppressing the internal strain and reducing irreversible capacity loss. Moreover, a higher requirement of the operation voltage was put forward to increase the energy density of LIBs,[30] however, the Ni-rich NCM is more likely to undergo irreversible phase transitions, thus deteriorating the electrochemical performance. As shown in Figure 4g, the

specific discharge capacity of the NCM90@ZTO-0 cathode degrades rapidly under 2.8–4.5 V (25 °C), only maintaining 162.6 mA h g^{-1} and 71.0% capacity retention after 100 cycles, which is caused by the severe anisotropic contraction/expansion of unit cell and release of lattice oxygen during the phase transformation as the material approaches full delithiation,[31] thus shortening the cycling life. As a comparison, the NCM90@ZTO-7 cathode still delivers a desirable specific capacity of 199.8 mA h g^{-1} with a capacity retention of 88.2%, indicating that such a surface modification can effectively suppress the irreversibility phase transformation and strengthen the bulk structure. To further assess the reversibility of phase transitions induced by lithium extraction/intercalation during cycling, dQ dV^{-1} curves of the NCM90@ZTO-0 and NCM90@ZTO-7 cathodes were examined (Figure 4e,f; Figure S16, Supporting Information). Both cathodes undergo similar phase transitions (H1-M-H2-H3), meanwhile, the reversibility of the H2-H3 transition is positively correlated to their cycling stability,[32] the undesired irreversibility induces unit cell strain and results in microcracks inside the cathode. It is clear that the NCM90@ZTO-7 cathode displays a more reversible H2-H3 transition upon cycling, signifying its lower strain and accumulation of stress in the cycling compared to the NCM90@ZTO-0 cathode.[33]

The cycling stability gap between the NCM90@ZTO-0 and NCM90@ZTO-7 cathode became more obvious when they were tested at 55 °C in the voltage of 2.8–4.3 V (Figure 4h). The NCM90@ZTO-0 cathode displays a rapid capacity decay, delivering a specific discharge- capacity of 148.6 mA h g^{-1} after 100 cycles with a capacity retention of 70.5%. The unstable structure of the NCM90@ZTO-0 cathode probably stems from surface parasitic reactions and following escape of the lattice oxygen, which result in irreversible degradation as the surface structure varies from layered to NiO-type rock-salt phase, the latter blocking the Li-ion transport.[34] Conversely, the NCM90@ZTO-7 still shows encouraging cycling durability and delivers a specific capacity of 192.4 mA h g^{-1}, corresponding to a capacity retention of 90.1% after 100 cycles under the same test conditions. The enhanced performance probably derives from the epitaxial ZTO cladding, which effectively protects the surface and maintains the lattice oxygen/transition metal structure by preventing the surface corrosion toward NCM90@ZTO-7. The electrochemical impedance spectroscopy (EIS) technique was employed to assess the role of ZTO modification of NCM90@ZTO-7 in the cycling, as shown in Figure S13c,d (Supporting Information), where the impedance patterns consist of a straight line at low frequency and two small semicircles at middle/high frequency, corresponding to the Warburg impedance (W_o), charge-transfer resistance (R_{ct}), and interfacial film resistance (R_f), respectively.[35] Figure 4i shows the fitted impedance values that the NCM90@ZTO-0 cathode shows a threefold increase over the NCM90@ZTO-7 cathode (156.1Ω vs 40.6 Ω). After 100 cycles, the NCM90@ZTO-0 cathode shows a rapidly increased R_{ct} from 156.1 to 377.1 Ω, while the NCM90@ZTO-7 shows a moderate increase from 40.61 to 191.3 Ω, demonstrating that the epitaxial ZTO coating effectively suppress electrode/electrolyte interfacial side reactions, in good agreement with the electrochemical results.

2.3. Structural and Morphological Changes in the Cycled NCM90@ZTO-X Cathodes

To further reveal the effect of ZTO surface modification toward the internal strain of $LiNi_{0.9}Co_{0.05}Mn_{0.05}O_2$ during delithiation, in-situ XRD characterization was performed to track the structural variation of the NCM90@ZTO-0 and NCM90@ZTO-7 samples in the voltage range of 2.8–4.5 V. As observed in **Figure 5**a,b, the $(003)_{H1}$ peak slowly shifts to lower angles upon charging and fully evolves to $(003)_{H2}$,[36] indicating an expansion of the lattice parameter c. Such a process is mainly attributed to the increased O—O repulsion with the removal of Li^+ from the Li layer. With further Li^+ extraction, the $(003)_{H2}$ peak moves rapidly to higher angles, accompanied by the evolution of the H2 to H3 phase and sharp contraction of the c-axis.[37] The lattice contraction above 4.19 V can be explained by the reduced repulsion along the c-axis in the O-Li-O plate, due to the shared negative charge transfer from oxygen to higher valence nickel ions. The (003) peak shifts for the NCM90@ZTO-0 and NCM90@ZTO-7 cathodes are 0.87 and 0.24° during the H2-H3 phase transition, respectively. The corresponding sudden contraction of the c parameter is −4.91% and −2.85% (Figure 5c), demonstrating a positive effect of the ZTO modification to mitigate the abrupt contraction. Furthermore, the unit cell volume variation of the NCM90@ZTO-7 caused by the anisotropic strain is 4.49%, less than that of the NCM90@ZTO-0 (7.32%, Figure 5d). This significant mitigation of structural evolution confirms that the synergistic effect of the ZTO coating layer and the Zr doping effectively suppress the anisotropic volumetric variation and internal strain during delithiation, thereby reducing the microcracks generation formation and showing significantly enhanced cycling stability.

The lattice strain evolution during delithiation has been further analyzed by multiphysics simulation (the calculation process is presented in Note S2, Supporting Information), where the model particle size distribution and lattice shrinkage data are derived from the corresponding cross-sectional SEM image and in situ XRD data. The lithium concentration and stress distribution α (x, y) for the NCM90@ZTO-0 and NCM90@ZTO-7 cathode after delithiation (i.e., charged) are presented in Figure 5f–j. There is a certain correlation between the distribution of Li^+ concentration and stress. It can be inferred that the internal strain originates from anisotropic shrinkage/expansion of the unit cell during the Li^+ intercalation and de-intercalation processes.[38] The computed spatial stress distribution of the NCM90@ZTO-0 exhibits a local accumulation accompanied by the inhomogeneous lithium concentration gradient during delithiation (Figure 5g), which leads to intergranular cracking. By comparison, the stress accumulation in the NCM90@ZTO-7 is greatly reduced (Figure 5j) as the reduction of Li^+ gradients and elimination of concentration polarization (Figure 5i), due to the lower expansion/contraction along the c direction in the particles, thus resulting in less delamination cracking along the basal plane. These results confirm that such a surface modification could dissipate the internal strain accumulation and anchor the lattice oxygen by building an epitaxial ZTO layer, eventually enhancing the structural stability of ultrahigh-Ni NCM particles.

The structural variation during the charge/discharge process is further evaluated by XRD analysis in the voltage range

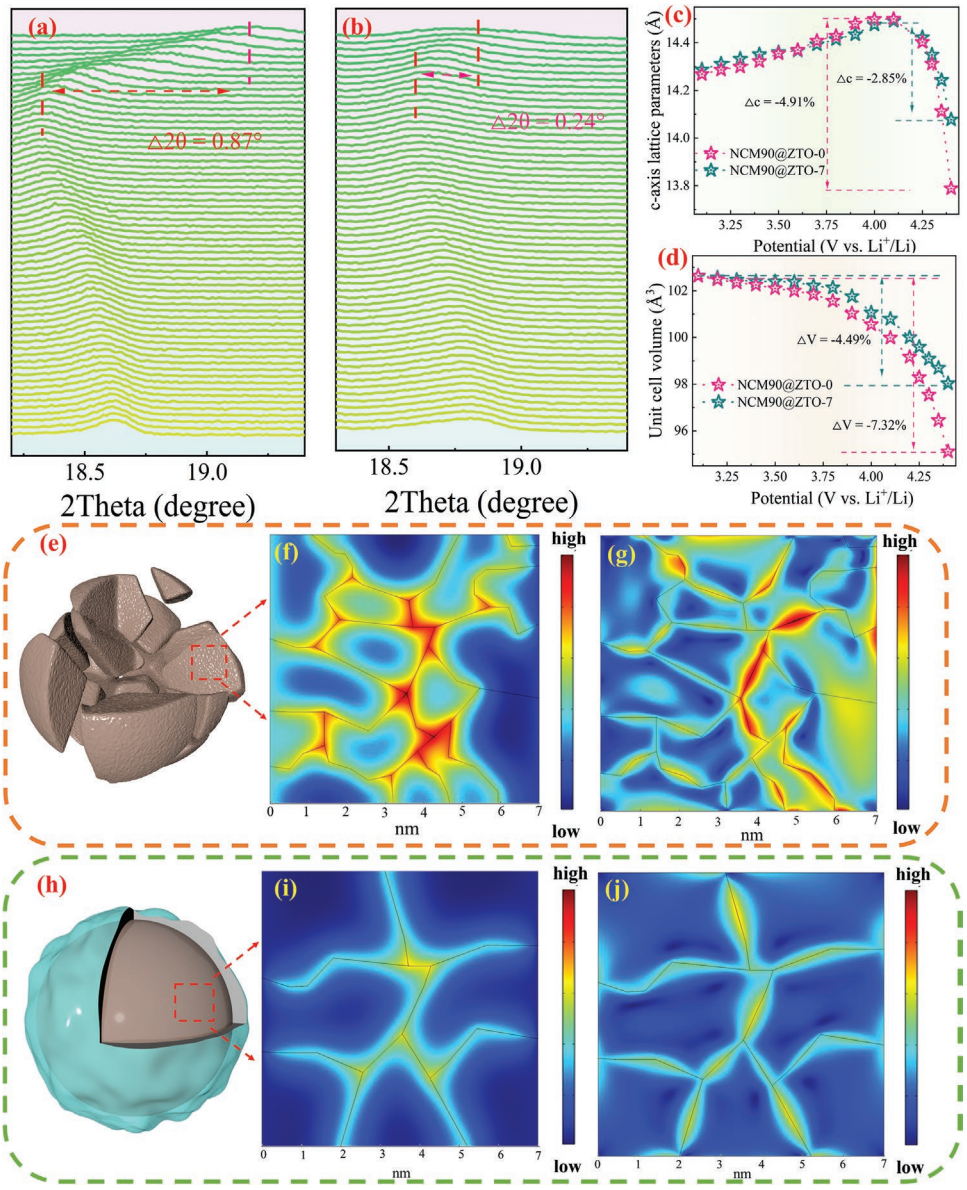

Figure 5. In situ XRD patterns of a) NCM90@ZTO-0 and b) NCM90@ZTO-7. Variation of unit cell parameters c) c and d) V as a function of voltage. Particle structure, lithium-ion concentration distribution, stress distribution for e–g) NCM90@ZTO-0 and h–j) NCM90@ZTO-7 at the state of deep delithiation.

of 2.8–4.5 V after 100 cycle and the significant differences are observed in the XRD patterns. The (003) reflection of the NCM90@ZTO-0 shifts by 0.33° toward lower angles, indicating that the NCM90@ZTO-0 has suffered serious irreversible structural degradation. In contrast, the NCM90@ZTO-7 displays a relatively lower shift of 0.11° after 100 cycles, as depicted in **Figure 6**a,b. The reason can be attributed to the fact that the epitaxial ZTO modification stabilizes the lattice oxygen and forms a stable crystal framework, which exhibits a shielding effect on the volume expansion/contraction behavior of the $LiNi_{0.9}Co_{0.05}Mn_{0.05}O_2$ during the H2-H3 phase transition. The particle morphologies of the two cathodes are also shown after 100 cycles in Figure 6d,e, Figures S17 and S18 (Supporting Information), where the changes in structure are clearly visible. The NCM90@ZTO-0 contains lots of microcracks, resulting from anisotropic volume variations during cycling,[3c] and these microcracks pulverize the particles into fragments, mainly accounting for the rapid decay of the NCM90@ZTO-0 cathode. In contrast, the spherical secondary particles of the NCM90@ZTO-7 cathode show limited microcracks, intuitively manifesting the positive effect of the ZTO layer on suppressing internal strain and maintaining structural integrity under the high-voltage operation. Meanwhile, benefiting from the enhanced mechanical structural stability of the ZTO surface modification, transition metal dissolution of the ZTO-modified samples is greatly reduced compared to the NCM90@ZTO-0 cathode, especially for Ni and Mn elements (Figure 6c).

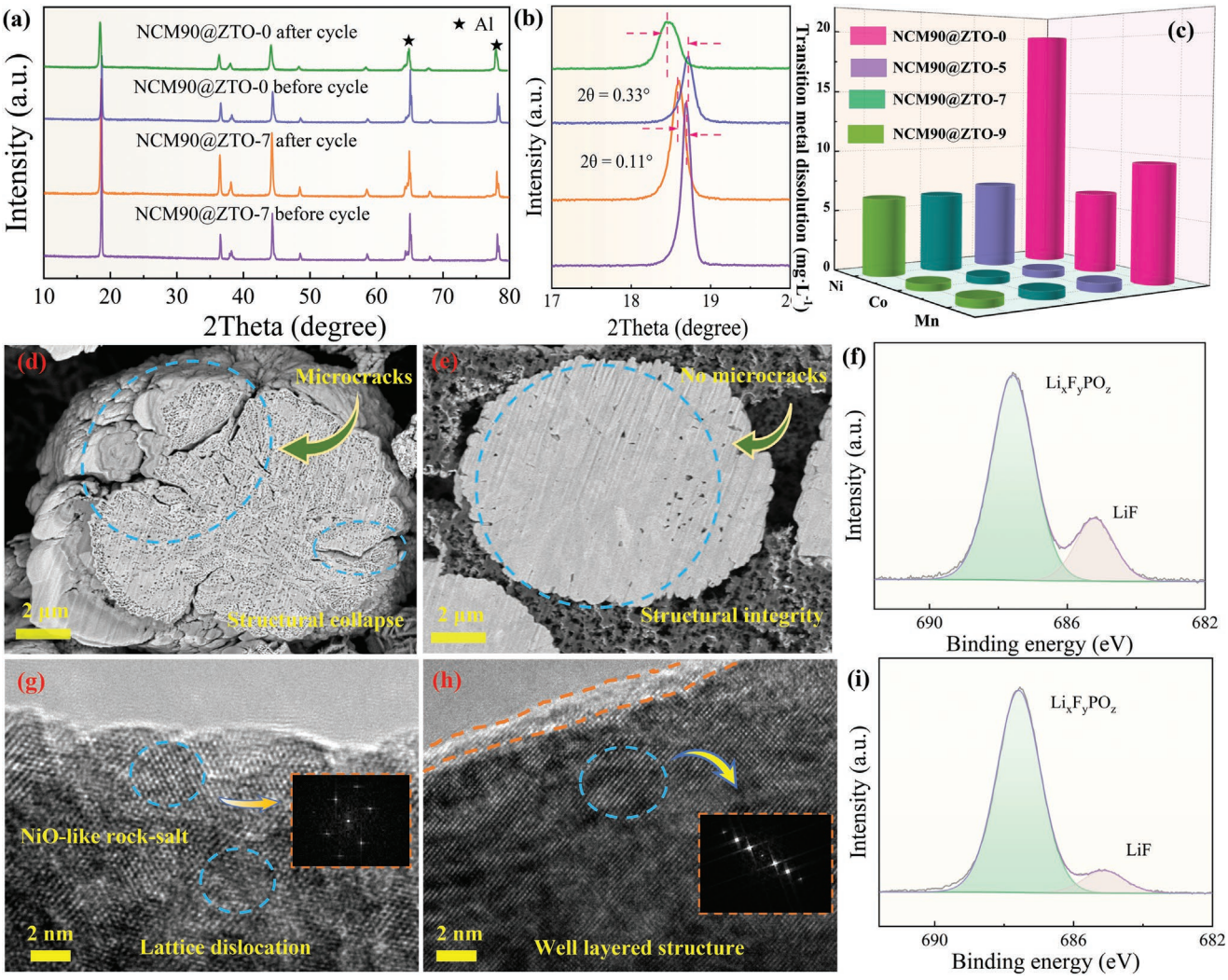

Figure 6. a) XRD patterns, b) magnified view of the (003) peak, and c) transition metal (TM) dissolution of the NCM90@ZTO-x cathode after 100 cycles. SEM images, HRTEM images, and F 1s spectrum for d,g,f) NCM90@ZTO-0 and (e,h,i) NCM90@ZTO-7 after 100 cycles.

HRTEM was used to evaluate differences in crystal structure of the NCM90@ZTO-0 and NCM90@ZTO-7 cathodes after 100 cycles in Figure 6g,h. The TEM image for NCM90@ZTO-0 shows a damaged crystal structure, and a noticeable rock salt phase (Fm-3m) region can be visually recognized in the internal structure of cathode, ascribed to the cation mixing and following oxygen release from the lattice during cycling.[39] In sharp contrast, the NCM90@ZTO-7 maintains clear lattice fringes and well-ordered layered structure, demonstrating that the ZTO modification effectively restrains irreversible transformation of the surface structure. Furthermore, F 1s XPS profiles of NCM90@ZTO-0 and NCM90@ZTO-7 were acquired to explore the parasitic reactions occurring at the cathode-electrolyte interface after 100 cycles at 4.5 V operation (Figure 6f,i). There are two characteristic peaks at 687.1 and 685 eV, corresponding to the components of $Li_xPF_yO_z$ and LiF, respectively[40] Lower LiF content interrelated to the decomposition of $LiPF_6$ is detected in the NCM90@ZTO-7 cathode, indicating that the ZTO protective layer prevents the corrosion (HF from the decomposition of electrolyte),[41] and helps maintain enhanced surface integrity and cycling stability.

2.4. Theoretical Analysis of Oxygen Vacancies

It is well known that lattice oxygen escapes from the bulk structure to form oxygen vacancies during heat treatment or high-voltage cycling, as exhibited in **Figure 7a**.[42] As the cycling proceeds (Figure 7b), such a local defect structure starts to induce large changes in the cell volume along the c-axis during the H2-H3 phase transition, resulting in severe lattice strain and microcracks. Thus, the oxygen release energy (E_{VO}) of the NCM90@ZTO-0 and NCM90@ZTO-7 cathode was acquired to evaluate the positive effect of the ZTO modification toward structural stability in Figure 7c. As calculated by density functional theory, the E_{VO} values of both cathodes exhibit a negative correlation with the removal rate of Li^+, and the E_{VO} values of NCM90@ZTO-7 are always higher than those

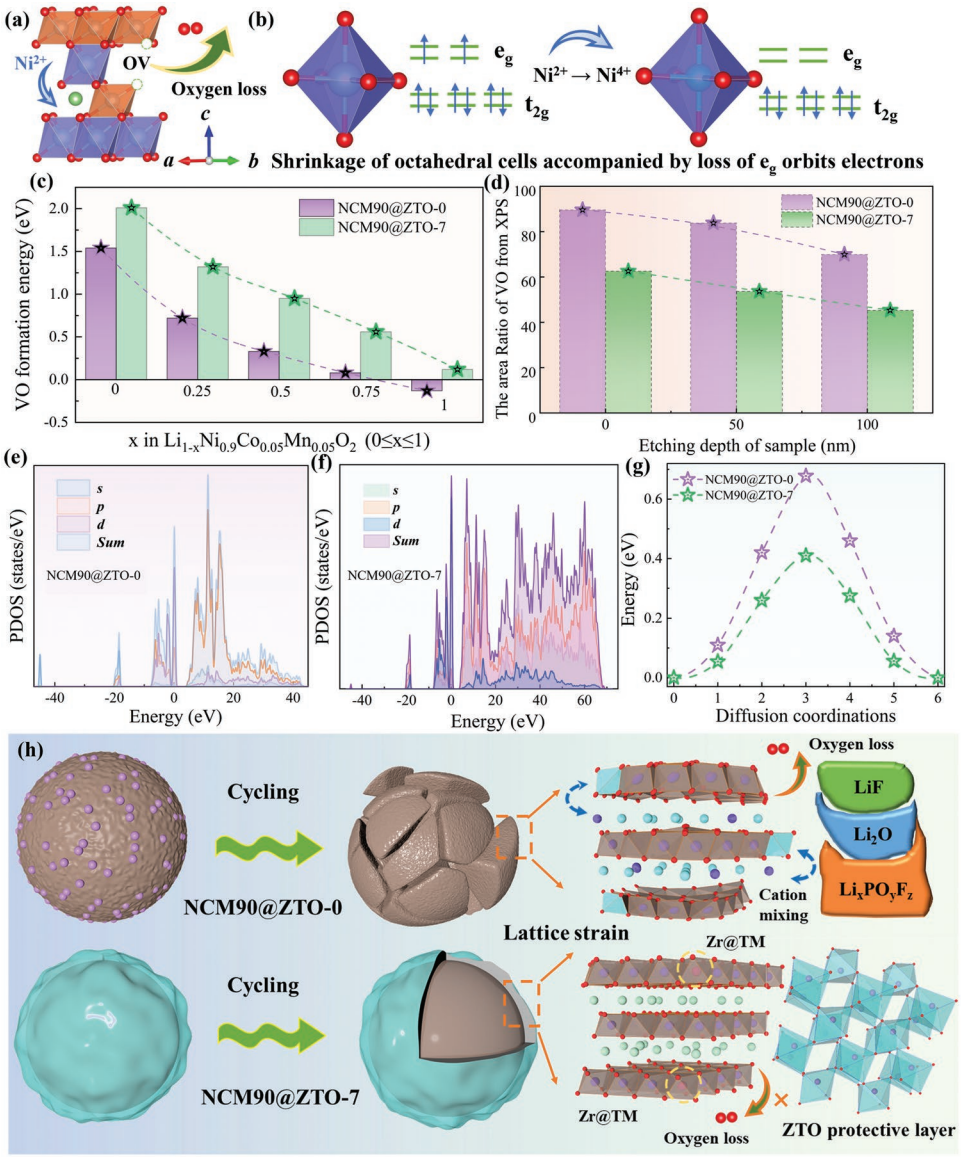

Figure 7. a) The oxygen loss and b) unit cell changes during charging of Ni-rich layered structure, c) VO formation, d) the ratio of VO of the cycled NCM90@ZTO-0 and NCM90@ZTO-7 cathode. Projected density of states (PDOS) of e) NCM90@ZTO-0 and f) NCM90@ZTO-7, g) Li-ion diffusion barrier, and h) schematic diagram for the degradation/improvement mechanism of NCM90@ZTO-0 and NCM90@ZTO-7.

of NCM90@ZTO-0 at different delithiation states. Specifically, a positive E_{VO} value is always maintained when the delithiation content is less than 75%, indicating that there is no lattice oxygen escape at this stage.[43] With a further extraction of lithium ions, the E_{VO} of the NCN90@ZTO-0 cathode drops to –0.13 eV, indicating that the lattice oxygen is automatically released from the NCN90@ZTO-0. In contrast, the E_{VO} of the NCN90@ZTO-7 cathode still remains at 0.12 eV, which directly demonstrates the inhibitory effect of the ZTO modification on the lattice oxygen release. As shown in Figure 7d and Figure S19 (Supporting Information), the area ratio of the VO peak in NCM90@ZTO-7 cathode is always less than that of the NCM90@ZTO-0 as the etch depth increases, further suggesting that the epitaxial ZTO coating is able to restrain irreversible loss of lattice oxygen upon cycling. In addition, due to the increased TM-O covalency, the area ratio of the VO peak decreases with the increasing of etch depth, revealing the propagation routine of the oxygen vacancy from surface to the bulk of particle.

To further unravel the underlying mechanism of the ZTO modification, electronic structure, and Li-ion diffusion of the NCM@ZTO-0 and NCM@ZTO-7 are discussed by the first-principles calculations. As shown the PDOS in Figure 7e,f, the total density of states illustrates that the bandgaps between the conduction band and valence band of the NCM@ZTO-0 and NCM@ZTO-7 are 2.66 and 1.76 eV, respectively, demonstrating the enhanced electrical conductivity of the NCM@ZTO-7, thus leading to the improved electrochemical performance of

the NCM90@ZTO-7 as shown in Figure 4. In layered NCM cathode, the Li-ion transfers between two octahedral sites by passing through a tetrahedral site. The lithium-ion diffusion barrier of the NCM90@ZTO-0 is 0.68 eV (Figure 7g), while that of the NCM90@ZTO-7 decreases to 0.40 eV, reflecting that such a surface modification engineering effectively reduces the Li^+ migration energy barrier and speed up the Li^+ transfer kinetic, consistent with the enhanced rate capability. Figure 7h summarizes the mechanisms of ZTO surface modification strategy to enhance crystal structure stability. The instability of the inherent structure of ultra-high Ni-rich layered materials will induce the severe internal strain and the lattice oxygen release to form an oxygen defect structure at the deep delithiation state. Subsequently, the local defect structure promotes the dislocations generation on the primary grains, leading to the formation of intergranular cracks and capacity decay of NCM90.[4a] Concurrently, with the increasing of Li^+ extraction, a serious cation mixing and the O-O dimers production originating from the oxygen defect structure leads to transition metal dissolution and rock-salt phase formation, further resulting in the collapse of the structure.[4b,c,31] Encouragingly, an active ceramic material of ZTO is employed to regulate the oxygen deficiency of $LiNi_{0.9}Co_{0.05}Mn_{0.05}O_2$ to maintain the structural integrity. Synergistic external and internal effects of ZTO cladding and Zr doping not only relieves lattice strain by avoiding inhomogeneity of the Li-ion concentration in the secondary spherical particles, but also anchors the lattice O to stabilize crystal structure for ensuring the smooth transportation of Li-ion, thus preventing the nucleation of intragranular fractures and following cracking formation. In addition, the ZTO coating provides a protective layer against electrolyte attack, which effectively suppresses parasitic side reactions on the electrode/electrolyte interphase, benefiting for excellent cycling capability.

3. Conclusion

In summary, a surface modification strategy to regulate the oxygen vacancy structure of Ni-rich $LiNi_{0.9}Co_{0.05}Mn_{0.05}O_2$ cathode and release the internal strain by using $ZrTiO_4$ as a surface modifier is proposed. Comprehensive structure variation and electrochemical characterization were carried out to reveal the working mechanism of the ZTO surface modification. It is found that the epitaxial ZTO layer is beneficial to construct a stable lattice structure for suppressing internal strain accumulation and oxygen release during the Li^+ de/intercalation, thereby preventing the intergranular cracking formation by guaranteeing homogeneous Li^+ distribution. As a result, the ZTO-modified $LiNi_{0.9}Co_{0.05}Mn_{0.05}O_2$ exhibits superior rate capability and cycling stability with remarkable capacity retention of 96.0% at 4.3 V and 88% at 4.5 V operation, far surpassing that of the unmodified $LiNi_{0.9}Co_{0.05}Mn_{0.05}O_2$ (79.4% and 71%, respectively). This work clarifies the regulation mechanism of surface modification engineering toward the intrinsic structural properties of ultrahigh-Ni NCM cathodes and sheds new light on the design and development of advanced high-energy LIBs.

4. Experimental Section

Materials Preparation of $ZrTiO_4$-Modified $LiNi_{0.9}Co_{0.05}Mn_{0.05}O_2$: For the preparation of the ZTO-modified $LiNi_{0.9}Co_{0.05}Mn_{0.05}O_2$, the 0.05 g mixture of $TiCl_4$ and $Zr(NO_3)_2$ (mol/mol = 1:1) was first dissolved in 100 mL absolute ethanol under strong stirring, and then 10 g $Ni_{0.9}Co_{0.05}Mn_{0.05}(OH)_2$ (spherical hydroxide precursor, Ningbo Rongbaixin Energy Technology Co., Ltd.) was gradually added under mild stirring. The mixture was then stirred at 80 °C overnight to evaporate the excess solvent. The acquired powder was grinded with $LiOH{\cdot}H_2O$ at the molar ratio of 1:1.05, then calcined at 500 °C for 5 h and 725 °C for 12 h to obtain the ZTO-coated NCM900505 cathode material. Three sets of samples with different coating amounts were prepared and named NCM90@ZTO-x (x = 5,7,9), where the mass ratio of ZTO and precursor was 0.5, 0.7, and 0.9 wt.%, respectively. Furthermore, the unmodified sample was processed by using the same calcination conditions without adding ZTO and is referred to as NCM90@ZTO-0.

Material Characterization: The powder crystal structure was analyzed by X-ray diffraction (XRD, Rigaku miniflex 600, Cu Kα radiation), where the crystal parameters of NCM90@ZTO-x were obtained through the Rietveld method by using GSAS software. In-situ XRD patterns were also collected on the charging process with at 0.2 °C rate (1 C = 200 mA g^{-1}) using the same device. The local chemical environment was investigated by X-ray photoelectron spectroscopy (XPS, Thermo ESCALAB 250XI), and the standard C 1s peak (284.8 eV) was used to calibrate the whole spectrum of the sample. Scanning electron microscopy (SEM, JEOL, JSM-7800F) equipped with an energy dispersive spectroscopy (EDS) system was used to investigate the surface morphology and element distribution of the NCM90@ZTO-x material. The formation and content of oxygen vacancies were probed using electron paramagnetic resonance measurements (EPR, Bruker ESR 5000) at a magnetic field modulation of 100 kHz. The crystal separation distance of the NCM90@ZTO-x was observed by the transmission electron microscopy (TEM, JEOL JEM-2100). The concentrations of residual lithium and transition metal dissolutions were identified by inductively coupled plasma optical emission spectroscopy (ICP-OES, Agilent ICPOES730). The soft X-ray absorption spectroscopy (XAS) measurements of the Ni L-edges and O K-edges were conducted at the Spherical Grating Monochrometer (SGM) beamline at the Hefei (China) Light Source. Details of the first-principles calculations and multi-physics-based analysis are provided in Notes S1 and S2 (Supporting Information), respectively.

Electrochemical Measurements: The cathode was prepared by mixing the NCM90@ZTO-x powders, polyvinylidene fluoride (PVDF) binder, and carbon black additive with a mass ratio of 8:1:1 in N-methyl-2-pyrrolidone (NMP) solvent and drying at 80 °C under vacuum for 12 h. The CR-2016 coin cells were assembled in an argon-filled glovebox, which contained one of the NCM90@ZTO-x electrodes with a 12 mm diameter as cathode, a lithium disk as anode, a Celgard 2325 separator, and 100 µL electrolyte consisting of 1 M $LiPF_6$ in EC (ethylene carbonate)-EMC (dimethyl carbonate) (1:1 vol%). The rate and cycling performance of the NCM90@ZTO-x cathodes were tested using a battery tester (CT3002A, LAND) at various rates (1 C = 200 mA g^{-1}) and cutoff voltages (2.8–4.3 and 2.8–4.5 V, vs Li^+/Li). Electrochemical impedance spectroscopy (EIS) measurement (frequency range: 0.1 Hz–1M Hz) and cyclic voltammetry (CV) at different sweep rates (0.1–0.5 mv s^{-1}) were carried out using the Princeton electrochemical workstation (VersaSTAT 4). The coin cells were first charged/discharged at 0.2 C for activation and then at 0.2 °C for the interval τ of 30 min to collect galvanostatic intermittent titration technique (GITT) data of the NCM90@ZTO-x cathodes.

Supporting Information

Supporting Information is available from the Wiley Online Library or from the author.

Acknowledgements

This work was financially supported by the Science and Technology of Guangxi Zhuang Autonomous Region (Gangxi special Fund for Scientific Center and Talent Resources:No. FA2020011 and FA20210713). The authors are grateful for resources from the High-performance Computing Center of Central South University and Shenzhen Puhua System Technology Co., Ltd for the DFT calculations. and the authors also thank Beijing Scistar Technology Co. Ltd for providing in-situ XRD test tool (LIB-XRD).

Conflict of Interest

The authors declare no conflict of interest.

Author Contributions

Z.T. and X.C. contributed equally to this work. Z.T. performed conceptualization, investigation, data curation, validation, and wrote the original draft. X.C. performed investigations, methodology, data curation, software, and validation. Y.L. performed supervision, project administration, provided funding acquisition, and reviewed and edited the final manuscript. X.X. performed validation and reviewed and edited the final manuscript. S.H., X.L., and X.S. performed data curation. Z.H. reviewed and edited the final manuscript. W.Z. performed conceptualization, supervision, and reviewed and edited the final manuscript. Y.Y. performed supervision and reviewed and edited the final manuscript.

Data Availability Statement

The data that support the findings of this study are available from the corresponding author upon reasonable request.

Keywords

chemo–electro–mechanical stability, intergranular cracking, internal strains, lattice oxygen, surface modifications

[1] a) L. Qiu, M. Zhang, Y. Song, Y. Xiao, Z. Wu, W. Xiang, Y. Liu, G. Wang, Y. Sun, J. Zhang, B. Zhang, X. Guo, *EcoMat* **2021**, *3*, e12141; b) A. Manthiram, J. C. Knight, S.-T. Myung, S.-M. Oh, Y.-K. Sun, *Adv. Energy Mater.* **2016**, *6*, 1501010; c) J. Kim, H. Lee, H. Cha, M. Yoon, M. Park, J. Cho, *Adv. Energy Mater.* **2018**, *8*, 1702028.

[2] a) Z. Tan, Y. Li, X. Xi, S. Jiang, X. Li, X. Shen, P. Zhang, Z. He, J. Zheng, *J Energy Chem* **2022**, *72*, 570; b) H.-H. Ryu, K.-J. Park, C. S. Yoon, Y.-K. Sun, *Chem. Mater.* **2018**, *30*, 1155.

[3] a) S. S. Zhang, *Energy Storage Mater.* **2020**, *24*, 247; b) S. Yin, W. Deng, J. Chen, X. Gao, G. Zou, H. Hou, X. Ji, *Nano Energy* **2021**, *83*, 105854; c) G. W. Nam, N.-Y. Park, K.-J. Park, J. Yang, J. Liu, C. S. Yoon, Y.-K. Sun, *ACS Energy Lett.* **2019**, *4*, 2995.

[4] a) Y. Su, Q. Zhang, L. Chen, L. Bao, Y. Lu, S. Chen, F. Wu, *J Energy Chem* **2022**, *65*, 236; b) W. Zhao, L. Zou, L. Zhang, X. Fan, H. Zhang, F. Pagani, E. Brack, L. Seidl, X. Ou, K. Egorov, X. Guo, G. Hu, S. Trabesinger, C. Wang, C. Battaglia, *Small* **2022**, *18*, 2107357; c) X. Fan, X. Ou, W. Zhao, Y. Liu, B. Zhang, J. Zhang, L. Zou, L. Seidl, Y. Li, G. Hu, C. Battaglia, Y. Yang, *Nat. Commun.* **2021**, *12*, 5320.

[5] a) C. Sun, X. Liao, F. Xia, Y. Zhao, L. Zhang, S. Mu, S. Shi, Y. Li, H. Peng, G. Van Tendeloo, K. Zhao, J. Wu, *ACS Nano* **2020**, *14*, 6181; b) S. Tao, W. Huang, S. Chu, B. Qian, L. Liu, W. Xu, *Mater. Today Phys.* **2021**, *18*, 100403; c) L. Li, J. Chen, H. Huang, L. Tan, L. Song, H.-H. Wu, C. Wang, Z. Zhao, H. Yi, J. Duan, T. Dong, *ACS Appl. Mater. Interfaces* **2021**, *13*, 42554.

[6] H. Wan, Z. Liu, G. Liu, S. Yi, P. Yan, H. Deng, W. Hu, F. Gao, *Nano Lett.* **2021**, *21*, 6875.

[7] C. Xu, W. Xiang, Z. Wu, L. Qiu, Y. Ming, W. Yang, L. Yue, J. Zhang, B. Zhong, X. Guo, G. Wang, Y. Liu, *Chem. Eng. J.* **2021**, *403*, 126314.

[8] L. Liang, W. Zhang, F. Zhao, D. K. Denis, F. u. Zaman, L. Hou, C. Yuan, *Adv. Mater. Interfaces* **2020**, *7*, 1901749.

[9] a) Y. Sun, W. Lv, P. Fu, Y. Song, D. Song, X. Shi, H. Zhang, C. Li, L. Zhang, D. Wang, *Chem. Eng. J.* **2020**, *400*, 125821; b) H. H. Sun, H.-H. Ryu, U.-H. Kim, J. A. Weeks, A. Heller, Y.-K. Sun, C. B. Mullins, *ACS Energy Lett.* **2020**, *5*, 1136.

[10] S. Jamil, M. Fasehullah, B. Jabar, P. Liu, M. K. Aslam, Y. Zhang, S. Bao, M. Xu, *Nano Energy* **2022**, *94*, 106961.

[11] Q. Hu, Y. He, D. Ren, Y. Song, Y. Wu, H. Liang, J. Gao, G. Xu, J. Cai, T. Li, H. Xu, L. Wang, Z. Chen, X. He, *Nano Energy* **2022**, *96*, 107123.

[12] H. Yang, H.-H. Wu, M. Ge, L. Li, Y. Yuan, Q. Yao, J. Chen, L. Xia, J. Zheng, Z. Chen, J. Duan, K. Kisslinger, X. C. Zeng, W.-K. Lee, Q. Zhang, J. Lu, *Adv. Funct. Mater.* **2019**, *29*, 1808825.

[13] X. Qu, H. Huang, T. Wan, L. Hu, Z. Yu, Y. Liu, A. Dou, Y. Zhou, M. Su, X. Peng, H.-H. Wu, T. Wu, D. Chu, *Nano Energy* **2022**, *91*, 106665.

[14] G. Shang, Y. Tang, Y. Lai, J. Wu, X. Yang, H. Li, C. Peng, J. Zheng, Z. Zhang, *J. Power Sources* **2019**, *423*, 246.

[15] H.-x. Wei, L.-b. Tang, Y.-d. Huang, Z.-y. Wang, Y.-h. Luo, Z.-j. He, C. Yan, J. Mao, K.-h. Dai, J.-c. Zheng, *Mater. Today* **2021**, *51*, 365.

[16] P. Xiao, W. Li, S. Chen, G. Li, Z. Dai, M. Feng, X. Chen, W. Yang, *ACS Appl. Mater. Interfaces* **2022**, *14*, 31851.

[17] L. Qiu, Y. Song, M. Zhang, Y. Liu, Z. Yang, Z. Wu, H. Zhang, W. Xiang, Y. Liu, G. Wang, Y. Sun, J. Zhang, B. Zhang, X. Guo, *Adv. Energy Mater.* **2022**, *12*, 2200022.

[18] S. Lee, W. Jin, S. H. Kim, S. H. Joo, G. Nam, P. Oh, Y.-K. Kim, S. K. Kwak, J. Cho, *Angew. Chem., Int. Ed.* **2019**, *58*, 10478.

[19] S. Sivaprakash, S. B. Majumder, S. Nieto, R. S. Katiyar, *J. Power Sources* **2007**, *170*, 433.

[20] F. Wu, N. Liu, L. Chen, N. Li, Y. Lu, D. Cao, M. Xu, Z. Wang, Y. Su, *ACS Appl. Mater. Interfaces* **2021**, *13*, 24925.

[21] E. Salahinejad, M. J. Hadianfard, D. D. Macdonald, I. Karimi, D. Vashaee, L. Tayebi, *Ceram. Int.* **2012**, *38*, 6145.

[22] J. Qiao, X. Zhang, C. Liu, L. Lyu, Y. Yang, Z. Wang, L. Wu, W. Liu, F. Wang, J. Liu, *Nano-Micro Lett.*. **2021**, *13*, 75.

[23] E. Lee, S. Muhammad, T. Kim, H. Kim, W. Lee, W.-S. Yoon, *Adv. Sci.* **2020**, *7*, 1902413.

[24] P. Yan, J. Zheng, Z.-K. Tang, A. Devaraj, G. Chen, K. Amine, J.-G. Zhang, L.-M. Liu, C. Wang, *Nat. Nanotechnol.* **2019**, *14*, 602.

[25] a) L. Ni, S. Zhang, A. Di, W. Deng, G. Zou, H. Hou, X. Ji, *Adv. Energy Mater.* **2022**, *12*, 2201510; b) Y.-h. Luo, Q.-l. Pan, H.-x. Wei, Y.-d. Huang, L.-b. Tang, Z.-y. Wang, Z.-j. He, C. Yan, J. Mao, K.-h. Dai, X.-h. Zhang, J.-c. Zheng, *Nano Energy* **2022**, *102*, 107626.

[26] a) L. Wang, X. Lei, T. Liu, A. Dai, D. Su, K. Amine, J. Lu, T. Wu, *Adv. Mater.* **2022**, *34*, 2200744; b) S. Li, Z. Liu, L. Yang, X. Shen, Q. Liu, Z. Hu, Q. Kong, J. Ma, J. Li, H.-J. Lin, C.-T. Chen, X. Wang, R. Yu, Z. Wang, L. Chen, *Nano Energy* **2022**, *98*, 107335.

[27] B. Xiao, B. Wang, J. Liu, K. Kaliyappan, Q. Sun, Y. Liu, G. Dadheech, M. P. Balogh, L. Yang, T.-K. Sham, R. Li, M. Cai, X. Sun, *Nano Energy* **2017**, *34*, 120.

[28] Y. Su, L. Li, G. Chen, L. Chen, N. Li, Y. Lu, L. Bao, S. Chen, F. Wu, *Chin. J. Chem.* **2021**, *39*, 189.
[29] Z. Tan, Y. Li, X. Xi, J. Yang, Y. Xu, Y. Xiong, S. Wang, S. Liu, J. Zheng, *Electrochim. Acta* **2022**, *401*, 139482.
[30] Q. Fan, K. Lin, S. Yang, S. Guan, J. Chen, S. Feng, J. Liu, L. Liu, J. Li, Z. Shi, *J. Power Sources* **2020**, *477*, 228745.
[31] W. Zhao, J. Zheng, L. Zou, H. Jia, B. Liu, H. Wang, M. H. Engelhard, C. Wang, W. Xu, Y. Yang, J.-G. Zhang, *Adv. Energy Mater.* **2018**, *8*, 1800297.
[32] S. Yin, H. Chen, J. Chen, A. Massoudi, W. Deng, X. Gao, S. Zhang, Y. Wang, T.-W. Lin, C. E. Banks, S.-z. Qiao, G. Zou, H. Hou, X. Ji, *Chem. Mater.* **2022**, *34*, 1509.
[33] X.-M. Fan, Y.-D. Huang, H.-X. Wei, L.-B. Tang, Z.-J. He, C. Yan, J. Mao, K.-H. Dai, J.-C. Zheng, *Adv. Funct. Mater.* **2022**, *32*, 2109421.
[34] a) Q. Ran, H. Zhao, X. Shu, Y. Hu, S. Hao, Q. Shen, W. Liu, J. Liu, M. Zhang, H. Li, X. Liu, *ACS Appl. Energy Mater.* **2019**, *2*, 3120; b) X. Dong, J. Yao, W. Zhu, X. Huang, X. Kuai, J. Tang, X. Li, S. Dai, L. Shen, R. Yang, L. Gao, J. Zhao, *J. Mater. Chem. A* **2019**, *7*, 20262.
[35] D. Rathore, M. Garayt, Y. Liu, C. Geng, M. Johnson, J. R. Dahn, C. Yang, *ACS Energy Lett.*. **2022**, *7*, 2189.
[36] Z. Zhang, B. Hong, M. Yi, X. Fan, Z. Zhang, X. Huang, Y. Lai, *Chem. Eng. J.* **2022**, *445*, 136825.
[37] H. Yu, Y. Cao, L. Chen, Y. Hu, X. Duan, S. Dai, C. Li, H. Jiang, *Nat. Commun.* **2021**, *12*, 4564.
[38] N.-Y. Park, G.-T. Park, S.-B. Kim, W. Jung, B.-C. Park, Y.-K. Sun, *ACS Energy Lett.*. **2022**, *7*, 2362.
[39] S. H. Song, M. Cho, I. Park, J.-G. Yoo, K.-T. Ko, J. Hong, J. Kim, S.-K. Jung, M. Avdeev, S. Ji, S. Lee, J. Bang, H. Kim, *Adv. Energy Mater.* **2020**, *10*, 2000521.
[40] a) L. Mu, Z. Yang, L. Tao, C. K. Waters, Z. Xu, L. Li, S. Sainio, Y. Du, H. L. Xin, D. Nordlund, F. Lin, *J. Mater. Chem. A* **2020**, *8*, 17487; b) C. Zhang, J. Wan, Y. Li, S. Zheng, K. Zhou, D. Wang, D. Wang, C. Hong, Z. Gong, Y. Yang, *J. Mater. Chem. A* **2020**, *8*, 6893.
[41] Y.-D. Huang, H.-X. Wei, P.-Y. Li, Y.-H. Luo, Q. Wen, D.-H. Le, Z.-J. He, H.-Y. Wang, Y.-G. Tang, C. Yan, J. Mao, K.-H. Dai, X.-H. Zhang, J.-C. Zheng, *J Energy Chem* **2022**, *75*, 301.
[42] Y. Su, Q. Zhang, L. Chen, L. Bao, Y. Lu, Q. Shi, J. Wang, S. Chen, F. Wu, *ACS Appl. Mater. Interfaces* **2020**, *12*, 37208.
[43] J. Cheng, L. Mu, C. Wang, Z. Yang, H. L. Xin, F. Lin, K. A. Persson, *J. Mater. Chem. A* **2020**, *8*, 23293.